RESEARCH ARTICLE

Particle & Particle Systems Characterization
www.particle-journal.com

Optical and Structural Properties of Cuprous Oxide Shell Coated Gold Nanoprisms

*Dániel Zámbó, Dávid Kovács, and András Deák**

Cuprous oxide nanoparticles can be prepared with a great morphological control, and their composites with gold nanostructures are intensively studied owing to their catalytic performance. In this study, cuprous oxide shell growth on nanosized prism-shaped gold nanoparticles is investigated, where the core-particle morphology does not match the prototypical cubic or octahedral symmetry of the embedding cuprous oxide particle. It is shown that different shell morphology is obtained depending on the reducing agent used for the shell deposition. Strong reducing agent (hydrazine) leads to a multi-slab-like coating with smooth facets, while under milder conditions (hydroxylamine) a multi-grain coating is obtained. Successful realization of time-dependent spectroscopic and structural investigations indicate that in this latter case cuprous oxide shell growth is initiated site-selectively, namely in the highly curved regions of the particle, with a higher growth rate around the tips of the nanoprisms. This is supported by correlative single-nanoparticle spectroscopy/scanning electron microscopy measurements, that allow to establish the connection between the optical properties and the structure of these plasmonic/semiconductor core/shell nanoparticles.

1. Introduction

Engineered noble metal/semiconductor composite nanoparticles can combine plasmonic properties and charge generation/separation in a single entity, making them very attractive for studying and utilizing photoinduced charge carrier-related processes. Among these nanoparticle hybrids, the gold/cuprous oxide (Cu_2O) system combines the excellent stability of gold with the abundance of copper. Thanks to the tremendous increase in wet-chemical synthetic protocols over the last decades, the synthesis of high-quality cuprous oxide and gold nanoparticles with different shapes and sizes is well established.[1–3] Also, their hybrid structures like core/shell, core/satellite, etc. structures have been realized and investigated with respect to their optical and catalytic properties, as summarized in a recent review on this topic.[4] In multicomponent Au/Cu_2O heteroparticles, the interaction between the metal and the semiconductor domains enabled their application in various photoinduced, charge carrier-mediated processes. Depending on excitation energy (wavelength), these structures can make use of both hot charge carriers created in the metal domain and of the excitation of valence band electrons in the semiconductor.[5] It enabled the use of such composite nanoparticles in water splitting,[6] CO_2 reduction,[7,8] and photocatalytic decomposition processes.[9,10] Gold nanoprism-based Cu_2O heteroparticles were also demonstrated to be active in the reduction of CO_2 to (mainly) CO recently.[5] The morphology of pure Cu_2O nanoparticles – and hence the type of exposed facets – can be controlled by the synthesis conditions, e.g. varying the type and amount of the reducing agent that is needed to reduce the typical Cu^{2+} precursor. For example, to prepare Au/Cu_2O core/shell nanoparticles both hydrazine and hydroxylamine have been successfully applied,[10,11] with hydrazine being a more powerful reducing agent, significantly shortening the particle growth time. The resulting particle shape is governed by the ratio of the growth rates along the ⟨100⟩ and ⟨111⟩ directions.[12] Some of the early demonstrations of Cu_2O shell growth on gold nanoparticles have shown that despite the 4.5% lattice mismatch between the ⟨111⟩ planes of gold and Cu_2O, the shell grows epitaxially on the gold core, and shells on different core-particle morphologies can be successfully deposited.[13,14] The Cu_2O shell growth is assumed to proceed through an intermediate conformal 'cage' formation around the gold core by small Cu_2O nanoparticles, which are formed in the bulk at alkaline pH of the reaction solution and grow into a continuous shell at later stages of the process.[13] Naturally, the presence of the oxide shell around the gold core particle has a profound impact on its surface plasmon resonance. Regarding the particles' extinction spectrum, the coating induces a redshift of the cores' plasmon modes. As the real part of Cu_2O's refractive index is

D. Zámbó, D. Kovács, A. Deák
HUN-REN Centre for Energy Research
Konkoly-Thege M. út 29–33, Budapest 1121, Hungary
E-mail: andras.deak@ek.hun-ren.hu
D. Kovács
Department of Physical Chemistry and Materials Science
Faculty of Chemical Technology and Biotechnology
Budapest University of Technology and Economics
Műegyetem rkp. 3., Budapest H-1111, Hungary

The ORCID identification number(s) for the author(s) of this article can be found under https://doi.org/10.1002/ppsc.202400082

DOI: 10.1002/ppsc.202400082

relatively large (≈2.7) over the visible and near-infrared wavelength range,[15] even a thin shell on the gold core can induce a substantial redshift of the resonances. At the same time, with increasing cuprous oxide shell thickness, absorption bands associated with Cu_2O become dominating in the spectrum at shorter wavelengths and the core's redshifted plasmon modes become significantly damped.[16,17] These make optical spectroscopy a useful technique to verify shell formation and enable it to follow its temporal evolution.

In this work, the cuprous oxide shell formation on prism-shaped gold nanoparticles is investigated. It is clear from the literature that a neat shell morphology can be obtained around gold cores when the core morphology 'fits' the prototypical cubic or octahedral symmetry of the embedding cuprous oxide particle.[10,11,18] This, however, is not the case for prism-shaped gold cores. There are some related examples of triangular gold prism/Cu_2O particles, but the core is hundreds of nanometres in size (more like a platelet) with large shell thickness,[5,13] which is closer to coating a planar gold surface with cuprous oxide. It is interesting to investigate whether the cuprous oxide can be 'forced' to conformally wrap small, prism-shaped nanoparticles and how the optical properties and the morphology of the hybrid particles develop during the process. For this, two prototypical reducing agents (hydrazine and hydroxylamine) were used, and the deposited shell morphology and the particles' optical properties were investigated both at the ensemble and at the single particle level – the small particle size allowed investigations to be carried out in the visible wavelength range. Different shell growth pathways for the two reducing agents could be identified, which stem from the shell growth commencing at different surface sites of the gold nanoprisms.

2. Results and Discussion

2.1. Cuprous Oxide Shell Growth Using Hydrazine

Deposition of the cuprous oxide shell using hydrazine is rapidly completed owing to its strong reduction potential and the sample shows pronounced color change over the course of the reaction (Figure S1a, Supporting Information). This color change is reflected in the extinction spectra after the synthesis, where instead of the initial, fairly sharp nanoprism in-plane plasmon resonance plasmon peak dominated spectra, several broader peaks can be observed for the final particles (**Figure 1a**), whereby no large differences were seen for the investigated gold core amounts used (Figure S1b, Supporting Information). The largest extinction below 600 nm is due to the absorption of the deposited cuprous oxide, while the peak ≈1100 nm can be assigned to the redshifted in-plane dipole of the prisms. This redshift together with the increased damping also indicates an intimate contact between the gold core and the cuprous oxide shell. The successful shell growth around the prism-shaped cores is confirmed by the TEM image of the composite particles (Figure 1b), where a ca. 50 nm thick neat shell around the prisms is visible and apparently the shell is terminated by definite edges. The scanning electron microscopy (SEM) images (Figure 1c) also confirm that the particles have a smooth outer surface, but in contrast to transmission electron microscopy (TEM) and scanning transmission electron microscopy (where a 2D projection of the core/shell particles is visible), the scanning electron microscopy images reveal that the particles have a rather irregular and not so well-defined shapes as observed earlier for other gold/cuprous oxide core/shell nanoparticle types.[1,10,17,19,20] It has to be noted though, that in general for thinner cuprous oxide shells, a more irregular shell morphology was found earlier – irrespectively of the reducing agent

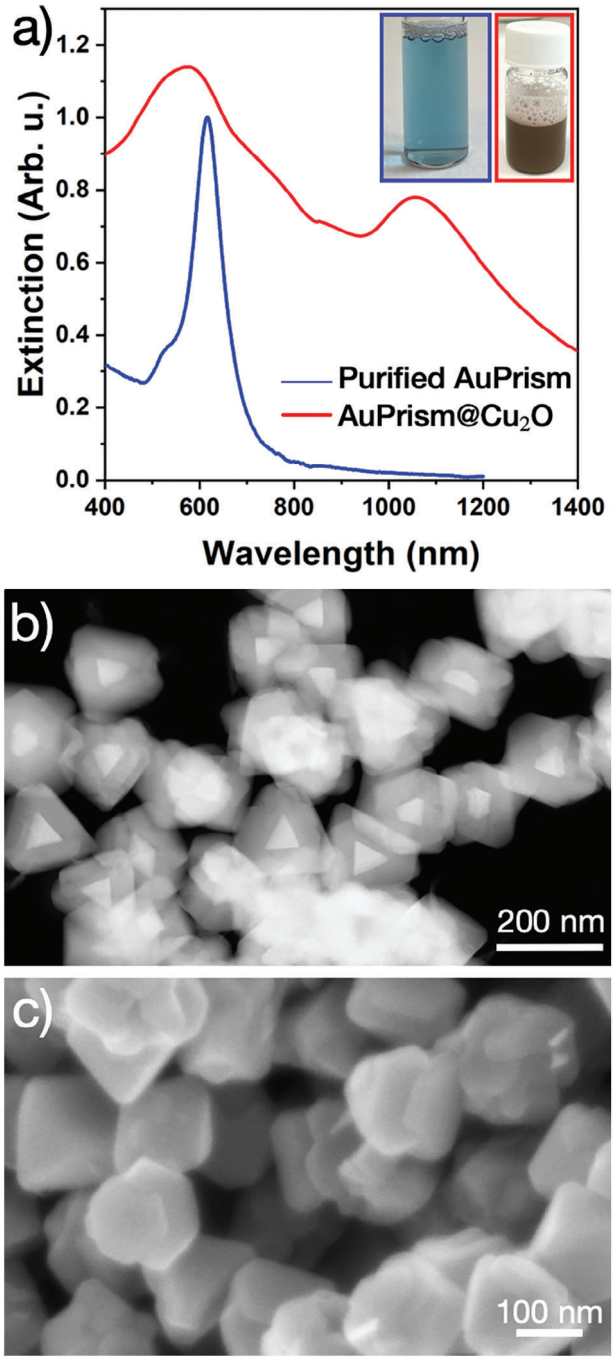

Figure 1. Extinction spectra of the Au@Cu_2O nanoprisms prepared using hydrazine as the reducing agent (70 nM final nanoprism concentration), the inset shows the corresponding sample images a). TEM b) and SEM c) micrographs of the core-shell particles.

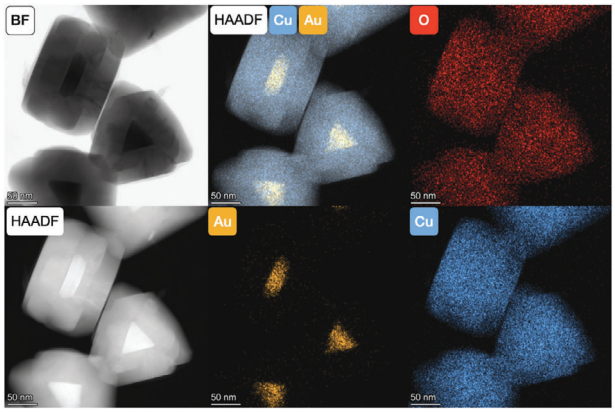

Figure 2. TEM, HAADF, and elemental maps of the core/shell particles prepared using hydrazine as the reducing agent.

used for coating the metal cores (hydrazine, hydroxylamine, or citrate).[21–24] Nevertheless, the triangular symmetry of the core can be observed in some cases also for the cuprous oxide coating, implying that it can direct the morphology of the deposited layer to some extent. At the same time, it is also evident (especially from the SEM images) that this core-replicated shell symmetry is not ubiquitous throughout the sample and looks like the coating of the particles is a composite shell consisting of several polycrystalline parts with different orientations, that can be attributed to the simultaneous growth starting in different directions.[13]

Close-up TEM investigation of a sample region, where by chance the core nanoprism with planar and vertical orientation can be observed simultaneously (**Figure 2**), reveals the nature of the shell inhomogeneity. When the core is oriented vertically (left in Figure 2), the slab-like morphology of the cuprous oxide coating becomes apparent. Also several 'sub-slabs' can be seen with interfaces parallel to the prism's planar faces. These sub-layers, however, might have a different orientation, as inferred from the irregularity of the flat laying and hence the top-imaged prism (right in Figure 2). Both the nanoprism orientation within the shell and the internal structure of the shell are corroborated by tilting the same sample in the (−20°)-(+20°) angle range (Figure S2, Supporting Information). The electron microscopic investigations hence suggest that shell growth predominantly takes place on the planar faces of the prisms and roughly follows the triangular symmetry of the cores. But as this symmetry is not favorable for cuprous oxide, nor is the shell deposition restricted to one side of the particle, the result will be an irregular overall particle morphology – a shell composed of layers and larger crystallites with different orientations.

2.2. Cuprous Oxide Shell Growth Using Hydroxylamine

Hydroxylamine was also employed for the shell growth as this milder reducing agent was considered to enable lower deposition rates and mitigate the irregular structure of the shell. Earlier studies have shown that for other core-particle morphologies, this approach can also lead to relatively thin (below 50 nm) shells on small (below 30 nm) spherical metal-core particles.[22,23] Indeed, also in the present case hydroxylamine-enabled reduction resulted generally in a slower shell growth on the minute time

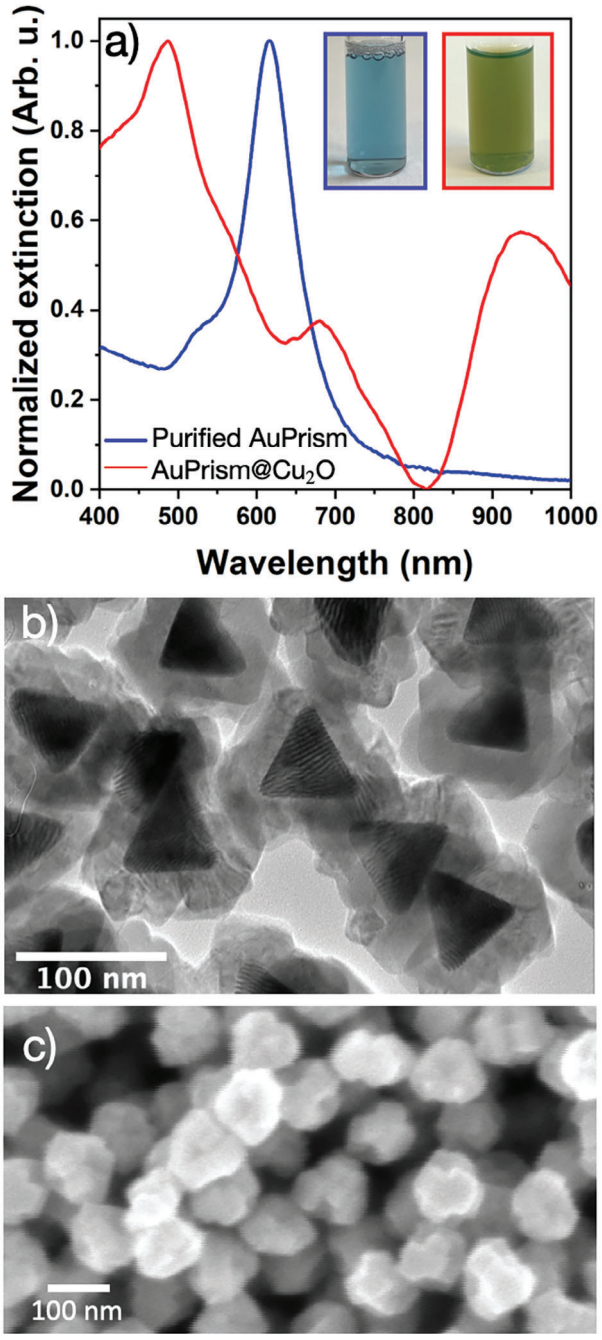

Figure 3. Normalized extinction spectra of the starting Au nanoprisms and the resulting core-shell structure prepared using hydroxylamine (final nanoprism concentration 29.2 nM), the inset shows the corresponding sample photographs a). TEM b), and SEM c) micrographs of the core-shell particles.

scale, and a smaller redshift is obtained for the prisms' dipolar resonance peak (**Figure 3a**). As the TEM images taken after the synthesis (Figure 3b) reveal, however, the ≈27 nm thick shell shows an even higher degree of inhomogeneity compared to hydrazine and together with the irregular edge shape indicates a multiple-grain structure of the shell. Moreover, the SEM images (Figure 3c) confirm that multiple small crystallites are

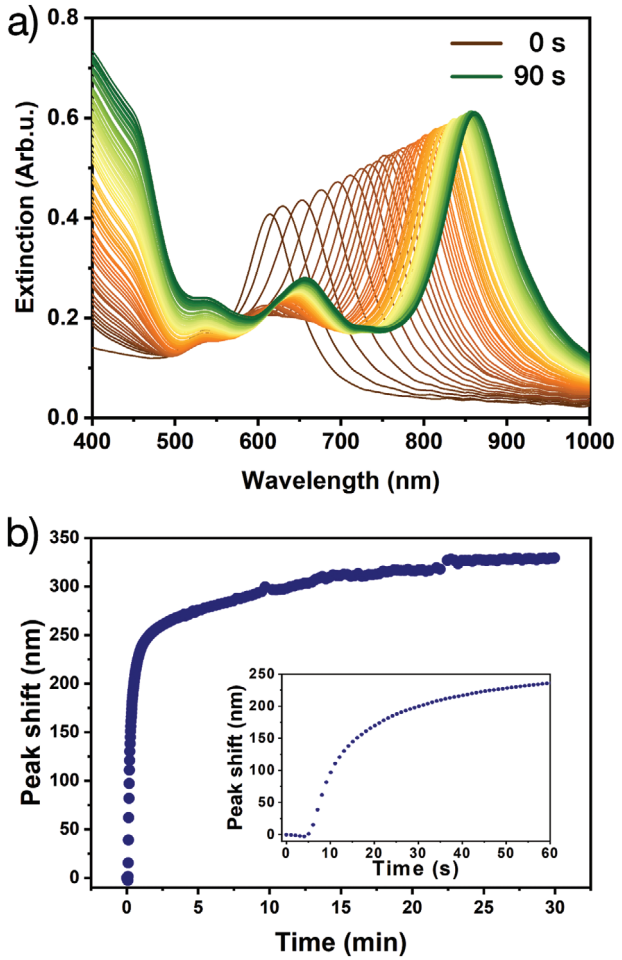

Figure 4. Time-dependent extinction spectra recorded during the shell growth in the first 90 s of the reaction; the spectra were recorded at 1 s time intervals a). Wavelength shift of the prisms' main dipolar plasmon peak over the 30 min reaction b); the inset provides an enlarged view of the first 60 s.

developing on the core particle. In contrast to the 2D projection in TEM, in the SEM images, the triangular shape is hard to recognize, suggesting a more complex 3D structure of the core-shell particles. It has to be noted that the standard approach to control the shell thickness in the system, namely to modify the amount of seed particles, cannot be realized beyond a certain point. When a smaller amount of prisms are present in the system, large particles are obtained with the simultaneous loss of shape homogeneity; the latter is also true when increasing the nanoprism amount above an optimum point (Figure S3, Supporting Information). Best results (fair size homogeneity together with well-developed crystalline domains) were obtained at 0.1575 mM final Au^0 concentration, corresponding to 29.2 nM nanoprism concentration. In order to investigate this structure evolution more in detail and identify the course of the shell development, time-dependent optical and structural investigations have been carried out.

Figure 4a shows the evolution of the extinction spectra during the first 90 s of the shell growth. The initial shell growth is rapid in this case as well, manifested in a quick redshift of the prism resonances. While the process slows down considerably after the first minute, there is still some redshift of the resonance up to 30 min (Figure 4b), accompanied by a significant peak broadening toward the end of the 30 min long shell growth process (Figure S4, Supporting Information). This latter indicates an increased damping of the surface plasmon resonance, owing to the absorptive nature of the shell material.

The overall spectral evolution as well as the appearance of the distinct spectral features can be well reproduced with calculations (**Figure** 5a). The calculated 331 nm wavelength shift of the prisms' dipole resonance at 27 nm shell thickness agrees well with the experimentally measured 330 nm redshift at the end of the growing process. Investigation of the surface polarization of the nanoparticles (Figure 5b) reveals that the band developing toward 660 nm in the experimental spectrum (toward 700 in the calculated one) can be assigned to a higher-order in-plane resonance of the core particles upon shell deposition. Below 500 nm the ever-increasing extinction with time can be assigned to the absorption of the shell material and the increasing scattering of the particle. This is also demonstrated when the simulated absorption and scattering contribution to overall extinction are examined (Figure S5, Supporting Information). In general, the extinction is dominated by the absorption of the particles. As expected, large plasmonic near-fields arise at wavelengths and excitation directions (relative to particle orientation) at the dipolar modes of the core particle: for in-plane excitation at ≈880 nm, for out-of-plane excitation ≈550 nm. The near-field distribution confirms the multipolar character of the intermediate peak and shows that the observed extinction increase with increasing shell thickness is mainly governed by absorption. Also, there are no significant plasmonic near-field present below 500 nm. In spite of the good agreement between the measured and calculated spectra, it is evident from the TEM images, that compared to hydrazine the hydroxylamine-grown shells are much more polycrystalline, suggesting that the shell growth takes place according to a different mechanism. To address this issue, the time-evaluation of the core-shell morphology in the presence of hydroxylamine has been investigated more in detail.

2.3. Single Particle Scattering and Structural Properties

Whereas for hydroxylamine the shell growth rate is slower compared to hydrazine, the reaction is still way too fast to allow for simple sampling of the course of the reaction. Therefore, carefully timed sampling was combined with quenching of the reaction: 100 µL from the reaction solution was taken and instantaneously injected into 9900 µL ethanol to stop the shell growth. The quenched sample was cleaned by centrifuging and redispersed in ethanol. **Figure** 6 shows the temporal evolution of the reaction together with corresponding TEM images. It is clear that the shell thickness increases over time, especially in the first 90 s (reaching 25 nm thickness), after which a largely reduced growth rate is observed. This reduced growth rate correlates well with the evolution of the spectral shift (Figure S6, Supporting Information), both indicating that the majority of the growth takes place within the first few minutes. Although the exponentially decaying nature of the near field around plasmonic particles implies that the extent of shift decreases with increasing shell thickness, the

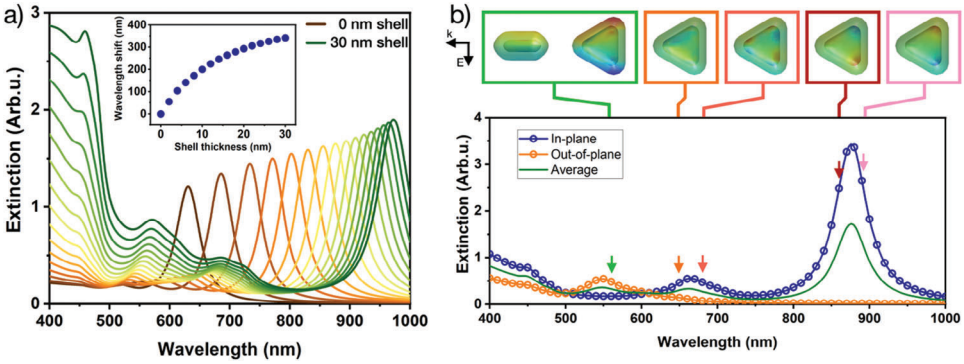

Figure 5. Simulated evolution of an AuPrism@Cu_2O conformal core-shell particle's extinction spectrum when the shell thickness is increased to 30 nm in 2 nm steps. The inset shows the wavelength shift of the prisms' main dipolar plasmon peak as a function of the shell thickness a). Simulated extinction spectrum of an Au@Cu_2O nanoparticle with a shell thickness of 14 nm. The upper panel shows the surface charge distribution on the particle (the shell is rendered semi-transparent for better visibility of the core), and the color coding is auto-scaled b).

simulations indicate that considerable peak shifts are expected in our system up to 30 nm shell thickness (see inset of Figure 5a). Hence, the observed saturation of the peakshift over time can be ascribed to the strongly reduced shell growth in the present case. This agrees well with the in-situ measured ensemble spectroscopic data, where the rate of redshift is strongly reduced after the first few minutes (Figure 4; Figure S4, Supporting Information). After this initial fast growth stage, the shell develops more homogeneously but does not gain much thickness anymore. The shell formation begins simultaneously around the whole perimeter of the nanoprisms, which would mean that the cuprous oxide shell growth in the presence of hydroxylamine fits into the big picture of nanoscale curvature-governed surface reactivity of nanoparticle, which was already demonstrated to be an excellent tool to control region-selective shell morphology or surface modification on nanoparticles.[7,25–27] This would also imply that especially at the very early stages of the process differences in the shell coverage of the edges/tip should be present or at least different shell growth rates in the curved (tips, edges) and flat (faces) regions of the prisms should apply. Unfortunately, as the TEM images represent only the 2D projection of the overall particle morphology and gold has a much larger contrast than the shell, this cannot be unambiguously determined from these measurements. Nevertheless, a close-up examination of the TEM images indicates based on the Moiré patterns (Figure S7, Supporting Information), that in the early stages of the growth (up to 45 s) multicrystalline Cu_2O domains are present primarily in the tip/edge region of the prisms. This transforms later (after 90 s) into a shell also covering the prisms' faces with an apparent restructuring, as the multiple orientation of the Moiré fringes observed in the beginning become more homogeneously oriented.

To provide this missing information, the very same quenched samples have also been subjected to correlated single-particle scattering spectroscopy/scanning electron microscopy experiments.

Figure 7 summarizes the typical results of the correlative measurements obtained for particles with different shell growth times (additional particle spectra and SEM images are provided in Figures S8–S10, Supporting Information). A clear trend with increasing shell growth time can be observed. The initial dipole

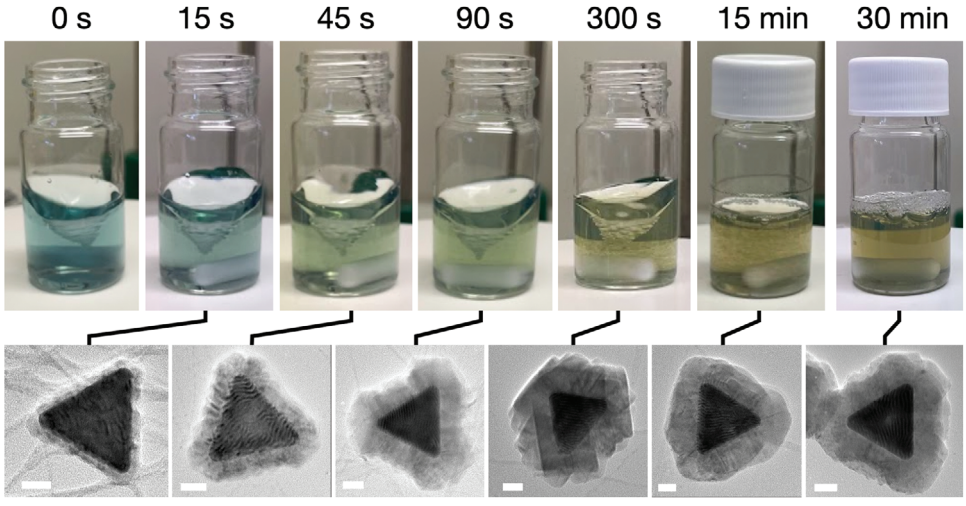

Figure 6. Snapshots of the reaction solution at different stages of the shell growth process (upper row) and the corresponding characteristic TEM images (lower row). Scale bars are 20 nm in all images, shell thickness changes from ≈7 to 27 nm.

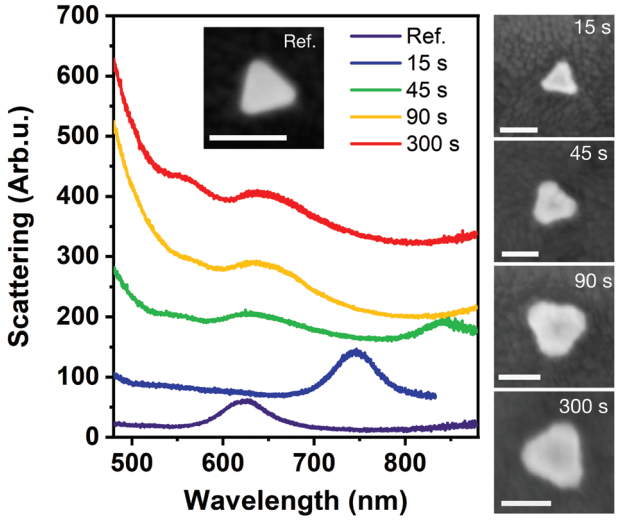

Figure 7. Typical single nanoparticle scattering spectra belonging to different stages of the shell growth process and corresponding SEM images. The spectra have been vertically shifted for clarity.

resonance associated scattering peak of the particles ≈630 nm agrees with the ensemble extinction peak of the prisms as the particles are supported by an ITO substrate. Already after 15 s of shell deposition time, the scattering peak shifts by ≈120 to 750 nm, which is in line with the ensemble spectral shift measured in situ in solution (Figure 4b). Further shell growth at 45 s into the reaction results in an even higher redshift, after which the resonance peak leaves our detection wavelength window. At the same time scattering peaks appear at ≈550 and 630 nm, which are in agreement with the ensemble measurement (Figure 4) as well as with the simulation results (Figure 5). They can be assigned to the increasing out-of-plane and higher-order in-plane modes of the particles. With increasing time, the scattering contribution at wavelengths below 550 nm also increases steadily. While these spectral features of the individual core-shell particles obtained after different growing times agree well with the in-situ measured ensemble spectral characteristics, the corresponding SEM images reveal a very important aspect of the shell growth process. It is clear that just like in the corresponding TEM pictures (Figure 6), the SEM images also indicate an increasing shell thickness as the shell growth reaction proceeds over time. More importantly, SEM confirms that for the present, hydroxylamine case, shell growth is more pronounced in the prism regions that have higher curvature – that is in the tip and edge regions of the particles and resembles the Cu_2O deposition at the edges of a few hundred nanometer-sized gold nanoplatelets.[5] For the 15 s and 45 s samples, a rim around the nanoprism perimeter is observed. Especially for the 90 s and 300 s samples, even a protrusion around the prism tips is visible, indicating that at these intermediate stages, the shell growth rate in the tip regions is higher compared to the edges or faces. A similar effect was also observed earlier for hydroxylamine-mediated cuprous oxide shells grown on region-selectively surface-modified gold nanorods.[7] Up until 90 s, the planar face regions of the prisms have a certainly lower shell coverage compared to the side/tip regions, which also agrees with the findings related to the TEM Moiré patterns. During the ensemble measurements, the pronounced peak broadening starts between 90 and 300 s (Figure S4, Supporting Information), hence it can be inferred that this marks the transformation of the rim-coated particle into a core-shell structure. This is reasonable as it has been shown earlier in many studies, that the surface-damping of the plasmonic resonance is due to the presence of adsorbed or deposited layers of scales with the affected surface area of the particles.[28] It should be noted that based on the shape transformation followed at the individual particle level, the cubic features observed in the SEM images of the final particles (Figure 3c) can be assigned to better-developed crystallites in the tip region of the nanoprisms.

3. Conclusion

While the gold nanoprism/cuprous oxide core-shell nanoparticles prepared using different reducing agents (hydrazine and hydroxylamine) share similar optical properties, there is a clear difference between the shell structure of the two particle types. The fast reduction in the presence of hydrazine leads to a multilayer-like cuprous oxide shell around the prisms, where the planar face region of the prisms seems to direct the shell growth since the different layers run parallel to the plane of the prism's face. Some of the layers can reproduce the triangular symmetry of the templating core, but the different layers are also rotated with respect to each other (and the core), resulting in an irregular, multi-grain overall core-shell particle morphology. For hydroxylamine, the shell growth is more pronounced in the curved regions of the prisms (edges and tips) especially in the early stage of the growth process, resulting in regionally inhomogeneous shell morphology, which is more polycrystalline than for the hydrazine case. At later stages pronounced crystallites can develop especially in the tip region of the core particle and an overall multi-faceted core-shell structure is obtained. For both systems, the optical properties are dominated by the presence of Cu_2O, redshifting the dipole resonance of the gold nanoprisms to the near-infrared and inducing a higher-order in-plane plasmon mode in the visible wavelength range.

4. Experimental Section

All chemicals were purchased from Merck and used as received. For the synthesis and purification of the particles, ultrapure water from a Sartorius Arium Mini was used.

Gold Nanoprism Synthesis: The gold nanoprisms have been synthesized and purified according to an already published protocol.[29] Two rounds of depletion-interaction assisted purification cycles were performed at 150 and 140 mM CTAC concentrations and the purified nanoprisms were stored at 50 mM CTAC concentration. The nanoparticles have an average dimension of 65 × 20 nm (edge-length×thickness).

Cuprous Oxide Shell Growth Using Hydrazine: For the hydrazine-mediated shell deposition, four different solutions were prepared: Solution A (0.0604 g $Cu(NO_3)_2$ + 0.721 g SDS + 20 mL water), Solution B (0.8 g NaOH + 10 mL water (2 M)), Solution C (0.125 mL N_2H_4 + 6.25 mL water) and the AuPrism dispersion (0.649 mM Au^0, 1 mM CTAC). 5 mL of Solution A, various volumes of AuPrism dispersion and 1.25 mL Solution B were combined and stirred for 15 min. Before adding 1.25 mL Solution C dropwise, the sample has been sonicated. After synthesis, the particles were centrifuged (3500 rcf; 10 min), the supernatant was completely removed and the precipitate was redispersed with 5 mL ethanol and sonicated for a few minutes. Water (5 mL) was then added to the dispersion and the centrifugation step was repeated once again in the same

manner (3500 rcf; 10 min). The precipitate was redispersed in 5 mL of ethanol, sonicated for a few minutes, and the final dispersion was stored in a refrigerator (6 °C) in dark conditions.

Cuprous Oxide Shell Growth Using Hydroxylamine: First, the Au^0 and CTAC concentration of the prisms was set to 0.315 and 0.222 mM, respectively. SDS (0.1 g) was dissolved in water (9475-x mL, "x" being the volume of the AuPrism solution to be added; 0.5–4 mL, Figure S3, Supporting Information). To this solution, $CuCl_2$ solution (50 µL; 0.1 M), various amounts of AuPrism solution, and NaOH solution (125 µL; 0.1 M) were added under continuous stirring at 250 rpm. The stirring speed was increased to 500 rpm before the rapid injection of NH_2OH•HCl solution (350 µL; 0.1 M). After 2 min, the stirring speed was reduced to 150 rpm. The nanoparticles were post-processed as written in the previous section.

Structural Characterization: Structural characterization was performed on a Zeiss LEO 1540-XB scanning electron microscope running at 5 kV acceleration voltage and an In-lens detector. TEM images and elemental maps were recorded using a JEOL 3010 microscope operated at 300 kV and a ThermoFischer THEMIS 200 transmission electron microscope operated at 200 kV, equipped with a spherical aberration-corrected objective lens and Bruker SuperX X-ray detectors. For electron microscopy 1 µL particle dispersion was drop casted on 3 × 2 mm Si wafers (SEM) or carbon-coated copper grids (TEM) and dried under ambient conditions.

Optical Characterization: For all measurements, cuvettes with 1 cm path length have been used. For the spectral characterization of the samples, a Shimadzu UV3600i Plus spectrophotometer was used. The Au^0 concentration was determined and adjusted based on the value measured at 400 nm.[30] For time-dependent extinction measurements, a Thorlabs CCS200 fiber coupled spectrometer and a Thorlabs SLS201 stabilized tungsten-halogen source connected to a CVH100 cuvette holder were used with a custom data acquisition software written in Labview. The cuvette holder was installed on a magnetic stirrer and the shell growth was performed in a standard macro cuvette, scaling down the total synthesis volume to 2.5 mL. A blackout paper with a hole installed in a CHV100-FH filter holder at the illumination side ensured that the stirring bar did not interfere with the light path. An integration time of the detector was set to 1 ms, and for each measurement, 100 spectra were averaged. In the first 5 min, spectra were taken every 1 s, then for the duration of an additional 25 min every 15 s.

Scattering Spectrum of Individual Nanoparticles: The nanoparticles were spin-coated on cleaned ITO substrates (PGO GmbH) (ultrasonication: 15 min in acetone, 15 min in 2-propanol, 15 min in water, 1 min air plasma treatment) at 3000 rpm. Single particle spectra were obtained on a laboratory-built workstation, consisting of an Olympus BX51 microscope, and an imaging spectrometer (Princeton Instruments Isoplane SCT320 + PIXIS 400 BRX camera running at −70 °C) as the main components. The software controlling the components and performing automatic measurements with position optimization was written in Labview. Dark-field illumination and collection of the particles' scattering spectra were realized with an Olympus 50× MPlanFLN (NA = 0.8) objective, illumination was provided by a 100 W Olympus U-LH100IR IR-enhanced light source. Precise positioning of the nanoparticles was ensured by a PI P-545.xR8S XYZ piezo-stage. Each particle's position was automatically optimized by the software to ensure identical measurement position, before taking the average of 3 spectra with 1 s exposure time each. All recorded spectra were inherently corrected by the optical transfer function of the setup (calibration performed by a NIST traceable wavelength and intensity calibration lamp from Princeton Instruments). To enable correlative scanning electron microscopy (finding the very same particles in SEM), pattern matching was used, and the scattering spectra of the particles were measured before SEM characterization to exclude contamination.

Calculation of Nanoparticle Spectra: The MNPBEM toolbox was used in Matlab to obtain the theoretical spectra of the nanoparticles, taking retardation into account.[31] The simulated gold nanoprisms had a dimension of 65 × 20 nm (edge-length and thickness), and the shell was considered conformal. The dielectric function of Cu_2O and gold was taken from the literature.[32,33] A homogeneous surrounding medium was set with a refractive index of 1.33. Two plane-wave excitation cases were implemented in terms of E-field oscillation (in-plane and out-of-plane of a horizontally positioned prism) and averaged (other geometries both in terms of the relative orientation of the particle and illumination direction as well as of the polarization direction can be reproduced by the linear combination of these cases).

Supporting Information

Supporting Information is available from the Wiley Online Library or from the author.

Acknowledgements

D.K. acknowledges the support of Pro Progressio and the József Varga Foundation. Project no. TKP2021-NKTA-05 has been implemented with the support provided by the Ministry of Innovation and Technology of Hungary from the National Research, Development and Innovation Fund (NRDI), financed under the TKP2021 funding scheme. The work received funding from the NRDI Fund of Hungary under the grants of FK 142148 and FK 128327.

Conflict of Interest

The authors declare no conflict of interest.

Data Availability Statement

The data that support the findings of this study are available from the corresponding author upon reasonable request.

Keywords

core-shell, cuprous oxide, gold nanoprism, microspectroscopy, optical properties

Received: April 25, 2024
Revised: June 6, 2024
Published online:

[1] Y.-C. Yang, H.-J. Wang, J. Whang, J.-S. Huang, L.-M. Lyu, P.-H. Lin, S. Gwo, M. H. Huang, *Nanoscale* **2014**, *6*, 4316.
[2] S.-C. Hsu, S.-Y. Liu, H.-J. Wang, M. H. Huang, *Small* **2015**, *11*, 195.
[3] J. Zhu, N. Lu, W. Chen, L. Kong, Y. Yang, D. Ma, S. Huang, *J. Nanomater.* **2015**, *2015*, 140716.
[4] E. D. R. Legaspi, M. D. Regulacio, *Nanoscale Adv.* **2023**, *5*, 5683.
[5] H. Jia, F. Li, T. H. Chow, X. Liu, H. Zhang, Y. Lu, J. Wang, C. Zhang, *Nano Lett.* **2022**, *22*, 7268.
[6] B. Wang, R. Li, Z. Zhang, W. Zhang, X. Yan, X. Wu, G. Cheng, R. Zheng, *J. Mater. Chem. A* **2017**, *5*, 14415.
[7] W. Xu, R. Xiao, S. An, C. Li, J. Ding, H. Chen, H. B. Yang, Y. Feng, *Small* **2023**, *19*, 2300587.
[8] B.-B. Zhang, Y.-H. Wang, S.-M. Xu, K. Chen, Y.-G. Yang, Q.-H. Kong, *RSC Adv.* **2020**, *10*, 19192.
[9] S. K. Cushing, J. Li, F. Meng, T. R. Senty, S. Suri, M. Zhi, M. Li, A. D. Bristow, N. Wu, *J. Am. Chem. Soc.* **2012**, *134*, 15033.
[10] D. Kovács, A. Deák, G. Z. Radnóczi, Z. E. Horváth, A. Sulyok, R. Schiller, O. Czömpöly, D. Zámbó, *J. Mater. Chem. C* **2023**, *11*, 8796.

[11] W. Xu, J. Jia, T. Wang, C. Li, B. He, J. Zong, Y. Wang, H. J. Fan, H. Xu, Y. Feng, H. Chen, *Angew. Chem. Int. Ed.* **2020**, *59*, 22246.
[12] H. Xu, W. Wang, W. Zhu, *J. Phys. Chem. B* **2006**, *110*, 13829.
[13] C.-H. Kuo, T.-E. Hua, M. H. Huang, *J. Am. Chem. Soc.* **2009**, *131*, 17871.
[14] Y. Q. Wang, K. Nikitin, D. W. McComb, *Chem. Phys. Lett.* **2008**, *456*, 202.
[15] S. Zhang, R. Jiang, Y.-M. Xie, Q. Ruan, B. Yang, J. Wang, H.-Q. Lin, *Adv. Mater.* **2015**, *27*, 7432.
[16] L. Zhang, D. A. Blom, H. Wang, *Chem. Mater.* **2011**, *23*, 4587.
[17] H.-J. Wang, K.-H. Yang, S.-C. Hsu, M. H. Huang, *Nanoscale* **2016**, *8*, 965.
[18] S. Zhang, R. Jiang, Y. Guo, B. Yang, X.-L. Chen, J. Wang, Y. Zhao, *Small* **2016**, *12*, 4264.
[19] W.-C. Wang, L.-M. Lyu, M. H. Huang, *Chem. Mater.* **2011**, *23*, 2677.
[20] C.-H. Kuo, Y.-C. Yang, S. Gwo, M. H. Huang, *J. Am. Chem. Soc.* **2011**, *133*, 1052.
[21] H. Jing, N. Large, Q. Zhang, H. Wang, *J. Phys. Chem. C* **2014**, *118*, 19948.
[22] S. Zhu, D. Deng, M. T. Nguyen, Y. R. Chau, C.-Y. Wen, T. Yonezawa, *Langmuir* **2020**, *36*, 3386.
[23] J. Li, S. K. Cushing, J. Bright, F. Meng, T. R. Senty, P. Zheng, A. D. Bristow, N. Wu, *ACS Catal.* **2013**, *3*, 47.
[24] D.-Y. Liu, S.-Y. Ding, H.-X. Lin, B.-J. Liu, Z.-Z. Ye, F.-R. Fan, B. Ren, Z.-Q. Tian, *J. Phys. Chem. C* **2012**, *116*, 4477.
[25] K. N. L. Hoang, S. M. McClain, S. M. Meyer, C. A. Jalomo, N. B. Forney, C. J. Murphy, *Chem. Commun.* **2022**, *58*, 9728.
[26] H. Duan, Z. Jia, M. Liaqat, M. D. Mellor, H. Tan, M.-P. Nieh, Y. Lin, S. Link, C. F. Landes, J. He, *ACS Nano* **2023**, *17*, 12788.
[27] A. Kim, S. Zhou, L. Yao, S. Ni, B. Luo, C. E. Sing, Q. Chen, *J. Am. Chem. Soc.* **2019**, *141*, 11796.
[28] S. A. Lee, S. Link, *Acc. Chem. Res.* **2021**, *54*, 1950.
[29] L. Scarabelli, L. M. Liz-Marzán, *ACS Nano* **2021**, *15*, 18600.
[30] W. Haiss, N. T. K. Thanh, J. Aveyard, D. G. Fernig, *Anal. Chem.* **2007**, *79*, 4215.
[31] U. Hohenester, A. Trügler, *Comput. Phys. Commun.* **2012**, *183*, 370.
[32] R. L. Olmon, B. Slovick, T. W. Johnson, D. Shelton, S.-H. Oh, G. D. Boreman, M. B. Raschke, *Phys. Rev. B* **2012**, *86*, 235147.
[33] T. Ito, T. Kawashima, H. Yamaguchi, T. Masumi, S. Adachi, *J. Phys. Soc. Jpn.* **1998**, *67*, 2125.

